Case Study for Tsunami Design of Coastal Infrastructure: Spencer Creek Bridge, Oregon

Citation	Yim, S. C., Wei, Y., Azadbakht, M., Nimmala, S., & Potisuk, T. (2015). Case study for tsunami design of coastal infrastructure: Spencer Creek Bridge, Oregon. Journal of Bridge Engineering, 20(1), 05014008. doi:10.1061/(ASCE) BE.1943-5592.0000631
DOI	10.1061/(ASCE)BE.1943-5592.0000631
Publisher	ASCE - American Society of Civil Engineers
Version	Version of Record
Terms of Use	http://cdss.library.oregonstate.edu/sa-termsofuse

Case Study for Tsunami Design of Coastal Infrastructure: Spencer Creek Bridge, Oregon

Solomon C. Yim, F.ASCE[1]; Yong Wei[2]; Mohsen Azadbakht[3]; Seshu Nimmala[4]; and Tanarat Potisuk[5]

Abstract: The absence of tsunami load provisions in coastal infrastructure design has led to unchecked resistance capacity of bridges against one of the most eminent natural hazards on the U.S. west coast. The Spencer Creek Bridge, which was completely rebuilt on the Oregon coast in 2009, is a unique example to demonstrate development and implementation of site-specific tsunami loads during the design stage. Two tsunami models, the Cornell Multigrid Coupled Tsunami model (COMCOT) and the Finite-Volume Wave model (FVWAVE), defined the flow fields from three rupture configurations postulated for a Cascadia earthquake, which has a moment magnitude of 9.0 consistent with the seismic design of the bridge structure. Although both models produce comparable surface elevations at the site, the finite-volume formulation of FVWAVE provides higher flow speed because of its capability to conserve momentum and mass even with formation of tsunami bores. The FVWAVE results define the input to the computational fluid dynamic module of *LS-DYNA*. The computed time history of the horizontal and vertical loads on the bridge deck, in turn, provide the input to a finite-element model of the bridge structure for capacity comparisons and damage analysis. It is concluded that the earthquake design specifications used for this particular bridge provide more than sufficient strength to resist the maximum tsunami horizontal force. The margin of safety is much smaller for the uplift force, but still remains in an acceptable range.
DOI: 10.1061/(ASCE)BE.1943-5592.0000631.

Author keywords: Bridge; Bridge design; Cascadia subduction zone; Finite-element method (FEM); Finite-volume method; Tsunamis; Tsunami load estimation.

Introduction

Highway bridges, as an important part of transportation and lifeline systems, have an important role in maintaining access to impacted areas after a natural disaster. Their performance during past tsunamis, however, exposes a critical vulnerability faced by coastal communities (Iemura et al. 2005; Yashinsky 2012). The 2011 Great East Japan Earthquake and Tsunami caused major damage to coastal infrastructure, including more than 300 bridges along the Tohoku coasts (Akiyama et al. 2012). Most of these bridges survived the earthquake, but were completely destroyed by the tsunami, indicating that seismic design criteria do not necessarily provide enough strength to resist tsunami loads. Field studies discovered multiple failure mechanisms of the bridges affected by the tsunami. Overturned bridge decks indicated large uplift force on their seaboard side because of buoyancy and inertia from the tsunami before the lateral force was fully developed to push them off the pile caps (Kawashima 2012). In addition to connection failure that resulted in unseating bridge spans, failure of the bridge piers was also reported (Maruyama et al. 2012).

The 2004 Indian Ocean Tsunami motivated laboratory studies of tsunami loads on bridge superstructures (Kataoka 2006; Sugimoto and Unjoh 2007; Kosa et al. 2010). These small-scale experiments utilized solitary waves generated by a wavemaker or bores developed by sudden releases of water from a storage tank. Kosa et al. (2010) reported that the location of the bridge with respect to the point where the wave breaks has bearing on the resulting forces. For the same height, a broken wave led to higher horizontal force, and an unbroken wave resulted in larger uplift force. Sugimoto and Unjoh (2007) found that a higher still water level gave rise to a larger uplift force on bridge superstructures. Bridge models slid off their supports when the drag force exceeded the deadweight and when the lift force was twice as large as the weight. Kataoka (2006) observed a sudden impulsive force on bridge models caused by the initial impact, followed by a slowly decreasing drag force. Wave breaking has a significant effect on the magnitude of the impulsive force. The results also showed a relatively steady downward force on bridge models toward the end of the load cycle. Further laboratory studies on a larger scale will be required to fully understand bridge behaviors during a tsunami.

Despite active research (Cheung et al. 2011; Yim et al. 2012, 2014), there is a lack of established procedures and standards for estimation of tsunami loads on bridge superstructures in engineering practice. Existing empirical formulas are limited to wind-generated waves with much smaller temporal and spatial scales than a tsunami (Bea et al. 1999; Douglass et al. 2006; Cuomo et al. 2009). A case study is presented to demonstrate the development and implementation of site-specific tsunami loads during the design of the Spencer Creek Bridge, Oregon. The paper is organized to illustrate the workflow of tsunami design for coastal bridges. The next

[1]Glenn Willis Holcombe Professor of Structural Engineering, School of Civil and Construction Engineering, Oregon State Univ., Corvallis, OR 97331 (corresponding author). E-mail: solomon.yim@oregonstate.edu

[2]Research Scientist, Pacific Marine Environmental Laboratory, National Oceanic and Atmospheric Administration, 7600 Sandy Point Way NE, Seattle, WA 98115. E-mail: yong.wei@noaa.gov

[3]Graduate Research Assistant, School of Civil and Construction Engineering, Oregon State Univ., Corvallis, OR 97331. E-mail: azadbakm@onid.orst.edu

[4]Graduate Research Assistant, School of Civil and Construction Engineering, Oregon State Univ., Corvallis, OR 97331. E-mail: nimmala@engr.orst.edu

[5]Engineer, Oregon Dept. of Transportation, 355 Capitol St. NE, Salem, OR 97301. E-mail: Tanarat.potisuk@odot.state.or.us

Note. This manuscript was submitted on January 22, 2014; approved on March 27, 2014; published online on May 13, 2014. Discussion period open until October 13, 2014; separate discussions must be submitted for individual papers. This paper is part of the ***Journal of Bridge Engineering***, © ASCE, ISSN 1084-0702/05014008(12)/$25.00.

section summarizes the bridge design and site conditions. The sections on modeling of great Cascadia tsunamis and tsunami flow fields and parameters provide a description of site-specific tsunami hazards and the modeling work to define the design flow conditions. The use of two tsunami models illustrates the effects of the numerical formulation on the results. The section on fluid loads on superstructure describes the implementation of two-dimensional computational fluid dynamics analysis of tsunami loads on the bridge deck, whereas the section on bridge resistance analysis provides a comparison between the tsunami loads and resisting capacity. This is followed by the conclusions in the last section, summarizing the lessons learned from the case study.

Fig. 1. Original and temporary bridges in the background and foreground (image by Solomon C. Yim)

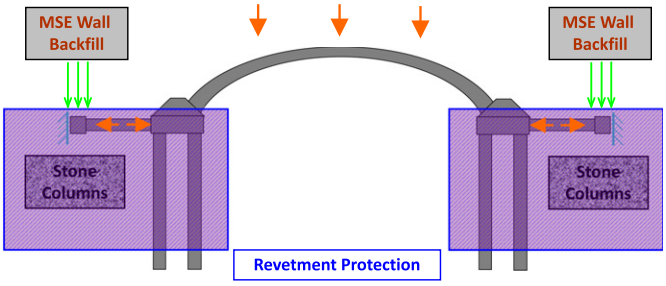

Fig. 2. Arch support and foundation systems

Spencer Creek Bridge

The Spencer Creek Bridge is on a segment of U.S. Highway 101 between Lincoln City and Newport, Oregon. The segment runs along the coastal dune system by the Pacific Ocean and serves as an important lifeline to local communities. The bridge provides the crossing over the outlet of Spencer Creek to the ocean. The alluvial plain landward of the bridge is a recreational park extending about 1 km inland. The original Spencer Creek Bridge, built in 1947, had deteriorated to the point that it was permanently closed to traffic by 2006. Fig. 1 shows the original and the temporary bypass bridge, which reached the end of its useful life in 2010. Design of the new Spencer Creek Bridge began in 2005 (Potisuk and McIntier 2009). The bridge has a 120-year design life. Because of its location in the Cascadia subduction zone, the seismic design utilized ground accelerations of 0.30 and 0.45g for the 500- and 1,000-year return periods, respectively. Because the bridge is located in a coastal region, considerations such as salt spray, tidal erosions, winter storms, and the silty sand and clayey silt at the bridge site were included in the design process.

The new bridge has an arch support system (Fig. 2). The arch, which has a span of 42.7 m (140 ft) and a rise of 9.6 m (31.5 ft), rests on pile caps supported by drilled shafts. Embedded thrust blocks supported by stone columns brace the arch backstops and resist the compressive loads through passive earth pressure. The stone columns reduce liquefaction-induced settlements and increase shear strength of the soil. Mechanically stabilized earth (MSE) walls at the bridge approaches reduce lateral spreading and improve stability during seismic events, whereas a revetment protects the foundation system from scour by stream flows and wave actions. Fig. 3 shows the main structural members. The bridge has six 15.6 m (51.25 ft) wide and 10.7 m (35 ft) long continuous spans with a total length of 36.6 m (210 ft). The superstructure consists of 0.30–0.46 m (12–18 in.) deep prestressed slabs with 0.13-m (5-in.) minimum concrete deck. The superstructure is located approximately 12.2 m (40 ft) above the stream bed. The cast-in-place concrete, used in the construction of the cross beams, closure pours, and shear lug, has a required strength of 29,992 kN/m^2 (4.35 ksi). The reinforcing dowel bars and dowels in

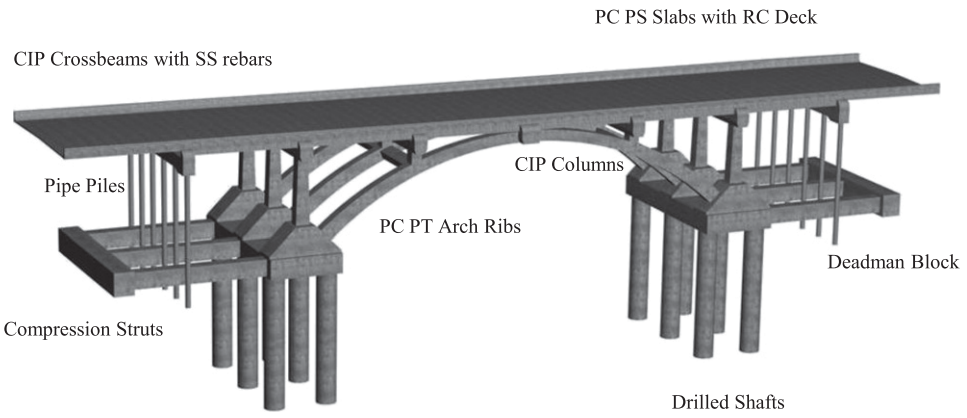

Fig. 3. Bridge structural members; CIP = cast in place; PC = precast; PS = posttensioned; PT = prestressed; SS = stainless steel

J. Bridge Eng. 2015.20.

the bridge superstructure are grade 75 stainless steel with a yield strength of 517,107 kN/m^2 (75 ksi).

A finite-element model provided a useful tool to assess and optimize the performance of the foundation and structural systems. Most of the load cases, such as deadweight, ground acceleration, traffic, and winds, are standard in bridge design manuals. Fig. 4 shows, for example, the deformed shape under the dead load. However, the Cascadia subduction zone is located less than 100 km offshore, and a catastrophic tsunami it generates can reach the bridge in 20–30 min. An additional design requirement calls for the structural capacity to withstand a tsunami having a compatible return period as the seismic loads. The analysis of tsunami impacts began in 2006, when a relatively complete design of the bridge became available. The abutments and stream bed are well protected from scour, and the structural members, which are constructed of high-strength concrete and steel, can sustain the drag forces from high-speed flows. The primary failure mode, as observed in Japan after the 2011 Tohoku tsunami, is unseating of the superstructure caused by overtopping by a tsunami. A secondary concern is the bending moment on the supporting columns because of the horizontal forces on the superstructure. The tsunami design, therefore, focused on the definition of the flow conditions at the bridge location and the corresponding hydrodynamic loads on the superstructure that, in turn, define the input load case in the finite-element model for assessment of the structural resistance.

Modeling of Great Cascadia Tsunamis

The Cascadia subduction zone extends 1,100 km along the Pacific coast from Northern California to British Columbia. Paleoseismological evidence indicates great earthquakes have an average recurrence interval of 500–600 years; the most recent event took place in 1700 (Clague 1997; Goldfinger et al. 2003; Jacoby et al. 1997). Satake et al. (2003) examined the magnitude and rupture zone of the 1700 Cascadia earthquake through tsunami records in Japan and North America. Comparison of the computed coastal wave heights with records of flooding and damage in Japan yielded three likely rupture scenarios with a moment magnitude of M_w 9.0. The long rupture covers the entire 1,100 km of the subduction zone, with average slip of approximately 14 m, whereas the short-north and short central ruptures of 670- and 360-km length have an average slip of 29 and 33 m, respectively. With the fault geometry and seismic source parameters from Kirby et al. (2006), the long, short-north, and short-central ruptures are, respectively, divided into four, three, and two rectangular faults for implementation of the planar fault model of Okada (1985). Fig. 5 shows the three rupture configurations and the earth surface deformations. The dip angle of the subduction zone gives rise to a skewed surface deformation with maximum uplift of 4.7, 6.7, and 12.2 m toward the ocean side for the long, short-north, and short-central ruptures, respectively. A large area of subsidence extends to the coastlines. The predicted subsidence values for the long, short-north, and short-central rupture scenarios at the bridge site are 2.76, 3.41, and 6.73 m, respectively. These values were taken into account in the calculations for tsunami flow conditions and loads on the Spencer Creek Bridge.

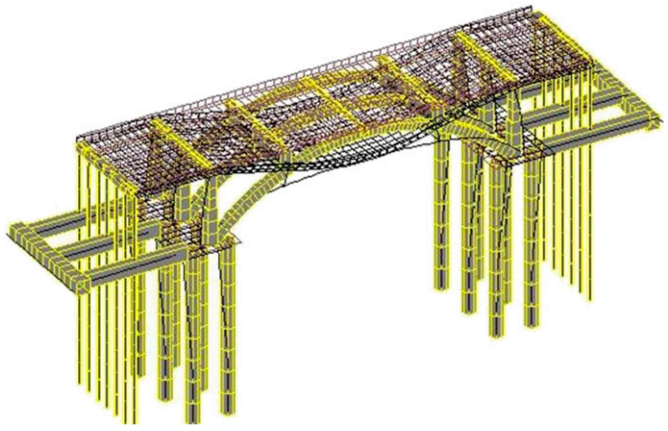

Fig. 4. Finite-element model and deformed shape under deadweight

The uplift and subsidence of the seafloor displace the ocean water and define the initial tsunami waveform (Kajiura 1970). Tsunami propagation across the ocean and inundation at coastlines can be described by various forms of the nonlinear shallow-water equations, which include a continuity equation and two momentum equations in two orthogonal directions defined on the ocean surface. Let h denote water depth, (u, v) the flow velocity, and the ζ the water surface elevation. The governing equations in the Cartesian coordinates (x, y) are

$$\frac{\partial \zeta}{\partial t} + \frac{\partial}{\partial x}(Hu) + \frac{\partial}{\partial y}(Hv) = 0 \tag{1}$$

$$\frac{\partial}{\partial t}(Hu) + \frac{\partial}{\partial x}\left(Hu^2\right) + \frac{\partial}{\partial y}(Huv) + gH\frac{\partial \zeta}{\partial x} + \frac{\tau_x}{\rho} = 0 \tag{2}$$

$$\frac{\partial}{\partial t}(Hv) + \frac{\partial}{\partial x}(Huv) + \frac{\partial}{\partial y}\left(Hv^2\right) + gH\frac{\partial \zeta}{\partial y} + \frac{\tau_y}{\rho} = 0 \tag{3}$$

in which the flow depth $H = h + \zeta$ and the bottom shear stress

$$\tau_x = \frac{gn^2}{H^{1/3}}u\left(u^2 + v^2\right) \tag{4a}$$

$$\tau_y = \frac{gn^2}{H^{1/3}}v\left(u^2 + v^2\right) \tag{4b}$$

where τ = time; ρ = water density; g = gravitational acceleration, and n = Manning number (Kowalik and Murty 1993; Liu et al. 1995; Titov and Synolakis 1998). The Cornell Multigrid Coupled Tsunami model (COMCOT) solves Eqs. (1)–(4) through an explicit finite-difference scheme with multiple levels of two-way nested grids (Liu et al. 1995). It utilizes the linear shallow-water equations to describe open-ocean wave propagation in spherical coordinates and the nonlinear equations for wave transformation and inundation in coastal regions. The moving waterline is realized by a staircase scheme, which floods or dries a boundary cell based on the flow depth at neighboring cells. The COMCOT provides accurate descriptions of tsunami propagation across the ocean and transformation around land masses. Wei et al. (2003) and Yamazaki et al. (2006) used this model to precompute mareograms for real-time tsunami forecasting and obtained very favorable predictions of coastal tsunami heights.

When dealing with discontinuities, volume conservation becomes an issue for the governing Eqs. (1)–(4). The finite-difference solution is not intended for situations when the seabed slope is steep or discontinuous, or when a bore develops. An alternative approach is to describe the flow using the conservative form of the nonlinear shallow-water Eqs. (1)–(4) as

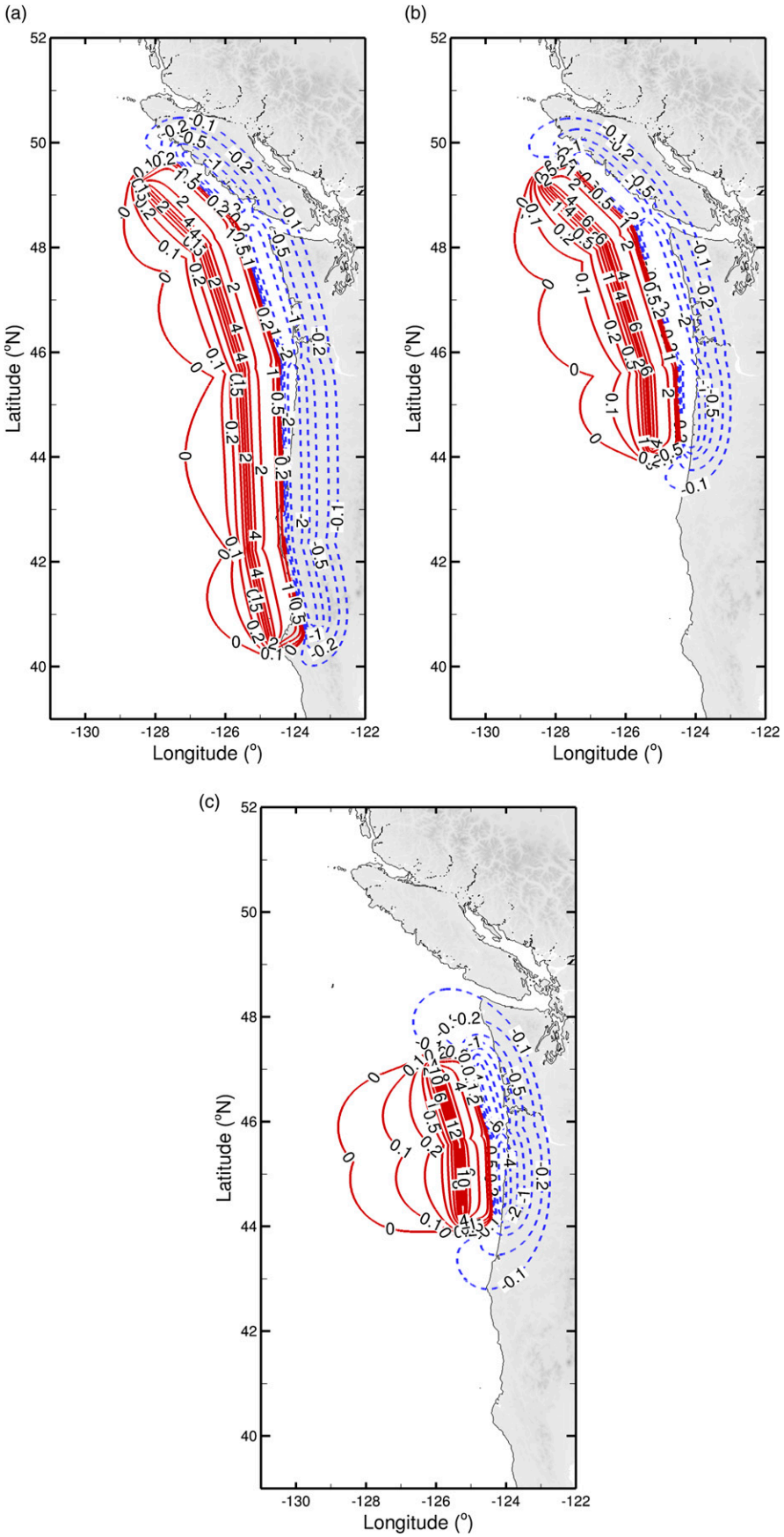

Fig. 5. Rupture configurations and earth surface deformation of the Great Cascadia earthquake: (a) long; (b) short-north; (c) short-central

$$\frac{\partial H}{\partial t} + \frac{\partial (Hu)}{\partial x} + \frac{\partial (Hv)}{\partial y} = 0 \quad (5)$$

$$\frac{\partial}{\partial t}(Hu) + \frac{\partial}{\partial x}\left(Hu^2 + \frac{gH^2}{2}\right) + \frac{\partial}{\partial y}(Huv) = gH\frac{\partial h}{\partial x} - \frac{\tau_x}{\rho} \quad (6)$$

$$\frac{\partial}{\partial t}(Hv) + \frac{\partial}{\partial x}(Huv) + \frac{\partial}{\partial y}\left(Hv^2 + \frac{gH^2}{2}\right) = gH\frac{\partial h}{\partial y} - \frac{\tau_y}{\rho} \quad (7)$$

The right-hand sides of the equations are known as the source terms in the finite-volume method, which solves the governing equations in integral form to provide a fully conservative scheme. The Finite-Volume Wave model (FVWAVE) developed by Wei et al. (2006) makes use of the surface-gradient method of Zhou et al. (2001) to provide a well-balanced formulation for the flux and source terms. A Godunov-type scheme with an exact Riemann solver is then used to track the moving waterline and to capture flow discontinuities associated with breaking waves, which are essential for inundation modeling. The scheme is second order in space and time, and provides an accurate description of small flow-depth perturbations near the moving waterline. The computed surface elevation, flow velocity, and runup show very good agreement with previous asymptotic and analytical solutions, as well as laboratory data. The advantage of FVWAVE is that it mimics breaking waves as bores and conserves volume across flow and bathymetry discontinuities in the nearshore region, whereas commonly used finite-difference models solving the nonconservative Eqs. (1)–(3) cannot conserve momentum and mass during discontinuous flow conditions. The conservative formulation formed the basis for subsequent development of dispersive wave models with shock-capturing capabilities (Roeber et al. 2010; Roeber and Cheung 2012; Yamazaki et al. 2009, 2011).

Two comparative approaches are used to compute the tsunami flow conditions at the bridge site. The first approach uses COMCOT to compute the tsunami generation, open-ocean propagation, and inundation at the bridge site. The computation involves three levels of nested grids with increasing resolution toward the site (Fig. 6). The level-1 grid over the eastern Pacific Ocean is around the Cascadia subduction zone. The water is deep, and the bathymetry varies gradually over most of the region. The selected grid size of approximately 1,000 m (0.5 min) optimizes the numerical diffusion to match the physical dispersion of a linear solution of the Boussinesq equations (Titov and Synolakis 1995; Burwell et al. 2007). Nonlinear effects become important, and finer computational grids are necessary as tsunamis approach land masses. The level-2 grid at approximately 100-m (3-s) resolution describes the tsunami transformation over the continental slope and shelf. The moving waterline is computed at this level to avoid the need to impose a minimum water depth and a vertical wall along the coastline. The level-3 grid covers a 10-km-long littoral cell bounded by headlands. The approximately 10-m (0.6-s) grid resolves the coastal dune system and alluvial plain to describe the inflow and outflow through Spencer Creek. The second approach utilizes FVWAVE instead of COMCOT at level 3 to capture tsunami bores and hydraulic jumps that might develop over shallow water or ponded areas. The bathymetry and topography are blended from the 1-min data set of Marks and Smith (2006), the 3-s National Geophysical Data Center Coastal Relief model, a National Oceanic and Atmospheric Administration (NOAA) Light Detection and Ranging (LIDAR) data set at 2-m resolution over a 300×150-m area at the bridge site, and the USGS Digital Elevation Model at 10-m resolution. The time steps of the computation are determined by the Courant-Friedrichs-Lewy criterion to be 0.4, 0.2, and 0.05 s for the three levels of grids.

Tsunami Flow Fields and Parameters

The finite-difference and finite-volume models provide a complete description of the tsunamis generated by the three possible rupture configurations of the Great Cascadia earthquake. The rupture is assumed to occur simultaneously over the entire fault. This is not necessarily the case for ruptures over long and narrow faults. In the absence of more detailed information, the assumption leads to more conservative tsunami events for the bridge design. Fig. 7 shows the wave-amplitude distributions generated by the short-central rupture. Although this configuration is not the most likely to occur, it produces the largest tsunami among the three and provides better correspondence with the seismic design criteria of up to a 1,000-year return period. The tsunami primarily affects the shoreline adjacent to the fault and has only minor impacts to the rest of the coast. Tsunami energy is known to propagate perpendicularly to the fault. The concave shapes of the fault focuses the energy toward the open ocean. The tsunami propagating toward the coast is focused over a number of submarine ridges before reaching the continental shelf. The tsunami approaches the coastline from the northwest because of refraction, and the wave amplitude reaches catastrophic levels on par with the 2011 Tohoku tsunami on the northeastern Japanese coasts (Yamazaki et al. 2013; Wei et al. 2003). The inundation is generally small because of the steep mountain slopes and coastal bluffs along the coastline, but extends deep into valleys and basins between mountain ridges. In particular, the floodwater overtops the coastal dune system and extends more than 1.4 km into the Spencer Creek basin.

The modeled tsunami flow conditions facilitate the structural and scour designs of the bridge. Fig. 8 shows the flow depth and velocity from both FVWAVE and COMCOT at mid span of the Spencer Creek Bridge. The flow depth is measured from the bottom of the creek, including effects of subsidence, and time zero is when the earthquake occurs. COMCOT predicts an arrival time of 13.5 min, which is 1.5 min earlier than FVWAVE. Both models show that the floodwater rises to 17 m above the creek bottom and overtops the bridge embankment, albeit with a time lag of 1.5 min. An inspection of the model results show transformation of the large initial wave into a bore in the shallow water within the level-2 grid, and is further intensified before reaching the shoreline at the level-3 grid. This is evident in the rapid increase of the flow depth before arrival of the peak at the bridge site. Roeber et al. (2010) demonstrated, through the Rankine-Hugoniot condition, that the conserved form of the nonlinear shallow-water Eqs. (5)–(7) used in FVWAVE can conserve momentum across discontinuous solutions and capture the shock speed, leading to the correct arrival time of the bore at the bridge. The u and v components of the depth-averaged velocity are positive in the east and north directions. The alignment of the bridge is north-south. The u component, which is perpendicular to the bridge, is critical to the bridge design. The flow increases with the arrival of the tsunami and reverses after the peak to discharge the floodwater from the creek basin back to the ocean. The outflow is quite steady because of the narrow outlet across the coastal dune and the large volume of water accumulated in the basin. The flow in the north-south direction corresponds to the refracted and reflected waves along the coast and the local alignment of the creek in the northwest direction toward the ocean.

The two models produce different flow velocity components despite the good agreement of the surface elevation. FVWAVE produces a maximum velocity of $(8, 3.5)$ m/s with a resultant speed of 8.7 m/s that coincides with the arrival of the initial wave. The prediction is consistent with the maximum flow speed of 10 m/s inferred from video recordings of the 2011 Tohoku tsunami at Kesenuma by Fritz et al. (2012) and preliminary model results of the inundation at Onagawa reported by Yim et al. (2014). COMCOT gives a maximum velocity of

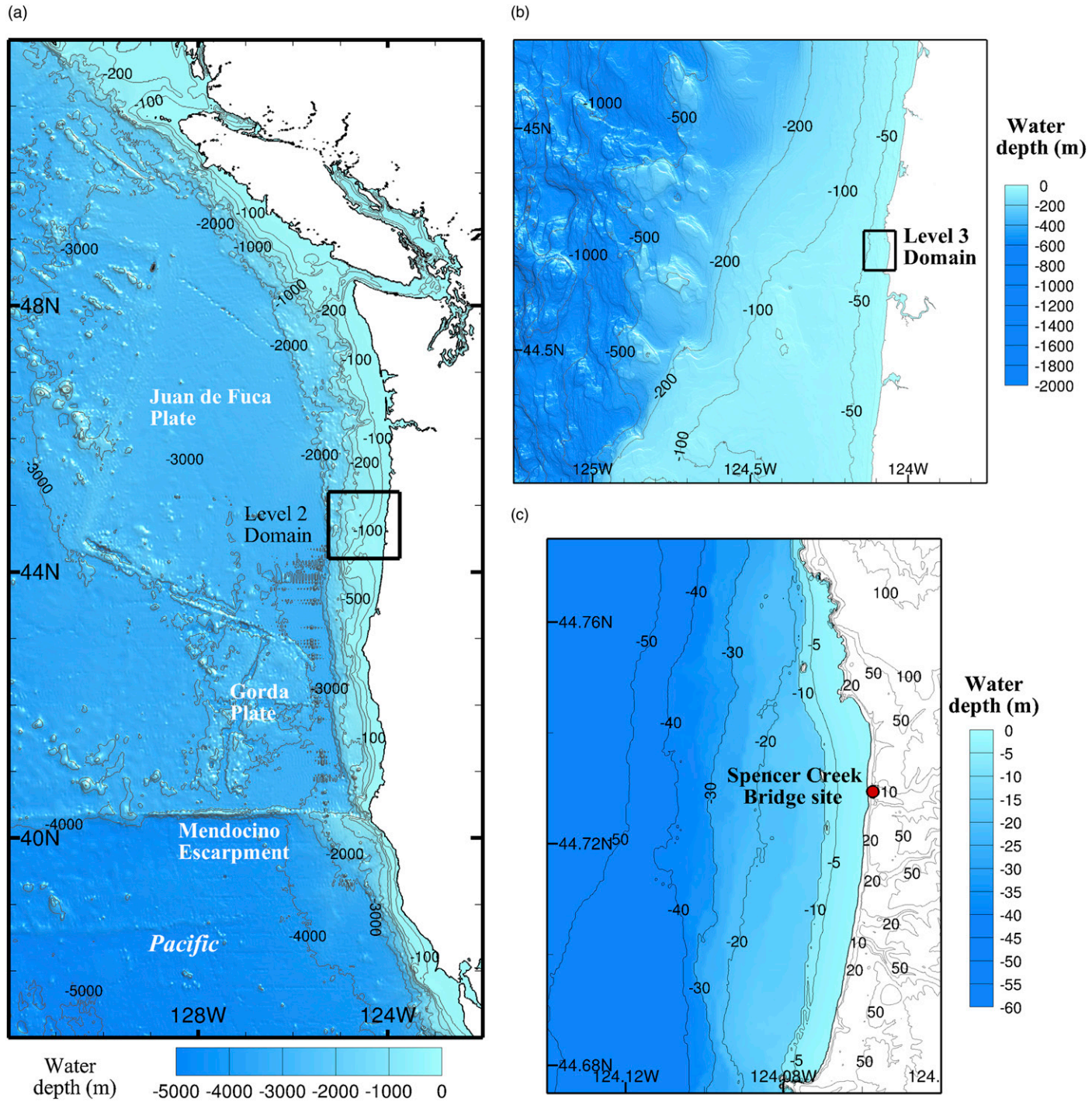

Fig. 6. Bathymetry and topography in computational grids: (a) level-1 eastern Pacific; (b) level-2 continental shelf; (c) level-3 littoral cell; labeled contours indicate the water depth in meters, rectangles indicate nested grids at the next level, and the dot identifies the bridge site

$(4.4, 2.2)$ m/s, with a resulting 4.9 m/s at the peak that is more than 40% lower in comparison. In addition, the u component develops a spike, and the v component shows high-frequency oscillations as the water surface elevation builds up rapidly, which is associated with the approaching bore just before the peak. The failure to conserve momentum across discontinuous solutions such as tsunami bores results in loss of volume and underestimation of flow speed and inundation. The lower flow speed and depth from COMCOT during the discharge are indicative of a much smaller volume of water accumulated in the creek basin from the initial wave. The FVWAVE is able to capture local variations of the flow momentum and align the outflow along the creek in the northwest direction. Despite the use of a second-order scheme, the finite-volume runup model generates stable results over the rugged bathymetry and topography without artificial damping mechanisms or smoothing to define the flow parameter for bridge load analysis.

Fluid Loads on Superstructure

Fluid flows are traditionally described by the Eulerian formulation with a fixed and undeformed mesh, whereas solids and structures are

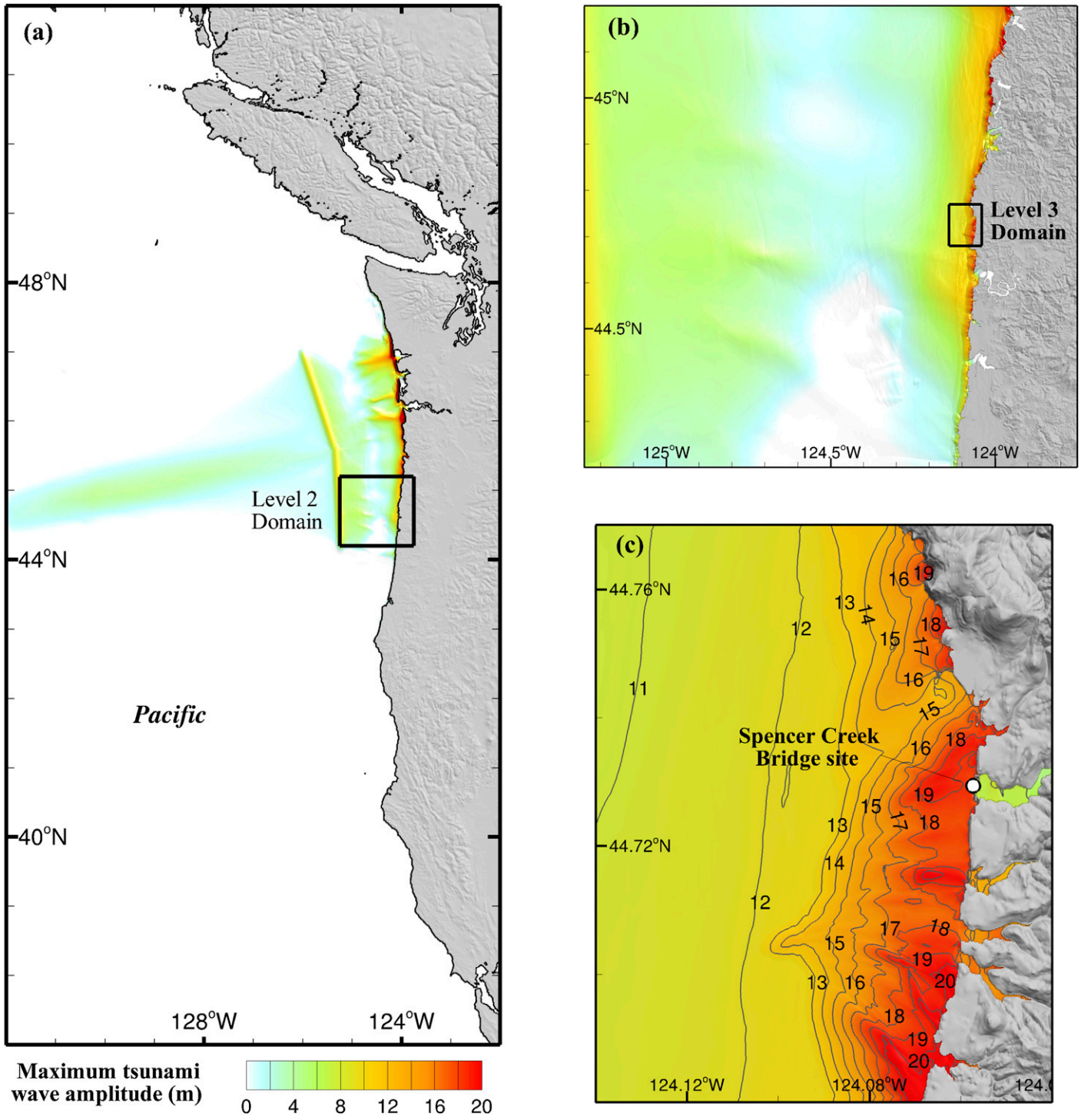

Fig. 7. Computed maximum tsunami wave amplitude of the Great Cascadia earthquake with the short-central rupture configuration: (a) level-1 eastern Pacific; (b) level-2 continental shelf; (c) level-3 littoral cell; labeled contours indicate the water depth in meters, rectangles indicate nested grids at the next level, and the dot identifies the bridge site

modeled using the Lagrangian approach, in which the mesh deforms and moves along with the material. The arbitrary Lagrangian Eulerian (ALE) formulation permits arbitrary motion of the mesh that has both the Eulerian and Lagrangian approaches as special cases. In addition, fluids are generally simulated using finite-difference or finite-volume techniques in contrast to structural analysis codes, which are almost based on the FEM. The Galerkin FEM (GFEM) is a generalized finite-volume method with rigorous mathematical analysis to form an ideal framework for modeling of the fully-coupled, fluid-structure interaction. A computational mechanics software, *LS-DYNA 971 R5*, which is a combination ALE and GFEM, is employed to simulate fluid loads on the bridge superstructure.

The tsunami flow is primarily perpendicular to the bridge, and the superstructure is the most vulnerable component of the structural system. A two-dimensional analysis of the superstructure cross

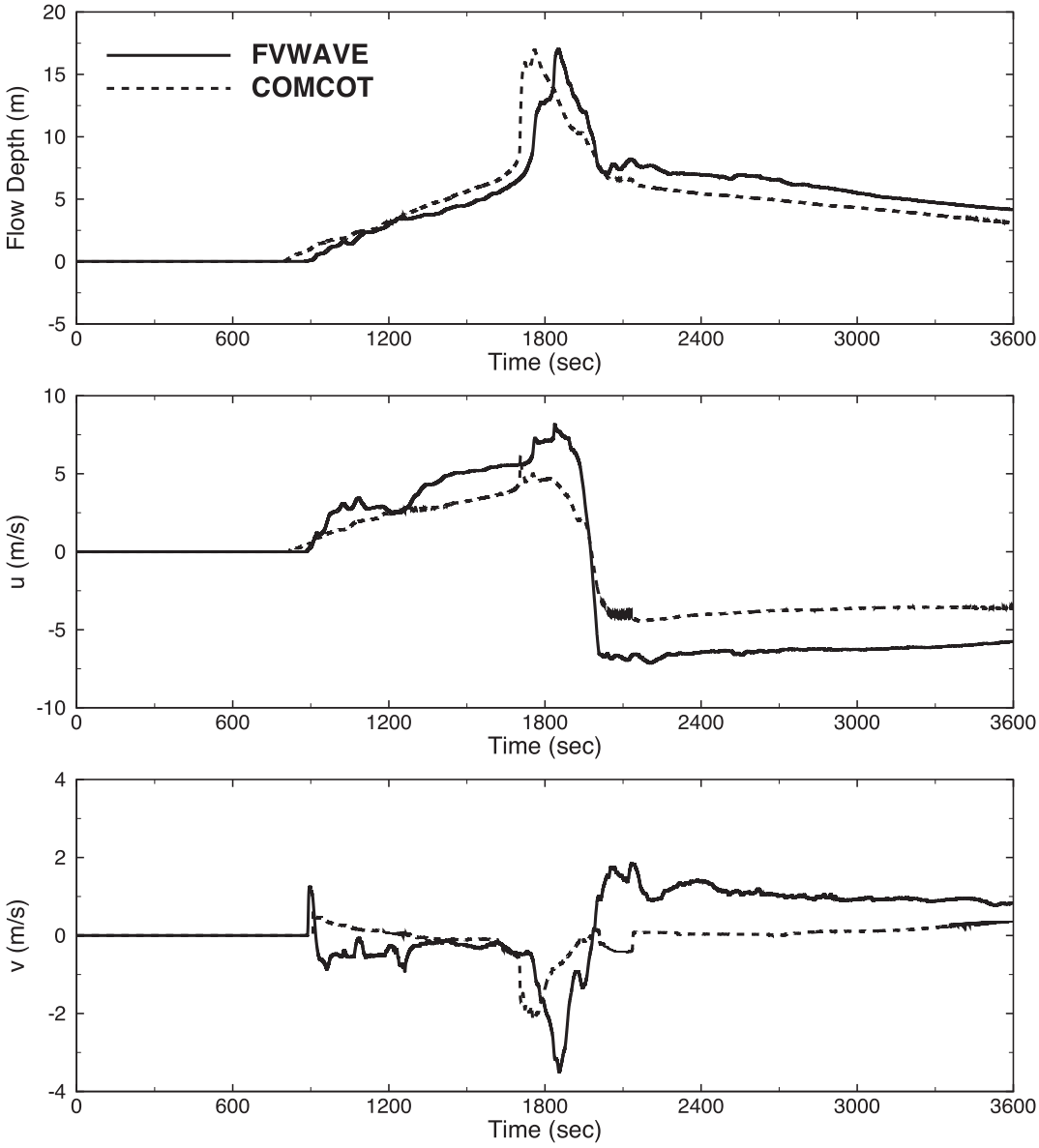

Fig. 8. Comparison of computed flow conditions at the bridge site from FVWAVE and COMCOT for the short-central fault configuration

section provides a conservative estimate of the tsunami loads. The railings are not included in the analysis. The finite-element model has approximately 74,000 nodes and 36,000 elements. *LS-DYNA* is capable of simulation fluid-structure interactions. Because the objective is to obtain the pressure and forces, the superstructure is modeled as rigid and fixed to minimize computational time. The simulation was performed for 60 s of the hydrograph around the peak flow when the tsunami overtops the superstructure. It took 29 h on 36 CPUs to finish the simulation. Fig. 9 shows screen captures of the simulation results. The flow depth and speed from the hydrograph is specified on the left and an open boundary on the right. Although the surface elevation rises and falls sharply during the episode, the flow velocity remains relatively steady between 7.5 and 8.0 m/s to the right. The superstructure obstructs the incoming flow and slightly lowers the water level downstream throughout the simulation. This is most evident at $t = 17.8$ s, when the swash over the superstructure re-enters the flow at the trailing edge with noticeable air entrainment. The submerged structure functions like a hydrofoil, modifying the free surface flow and creating a low-pressure wake.

Integration of the pressure yields the load time history to illustrate the effects of the tsunami on the superstructure. Fig. 10 plots the horizontal and vertical forces over the 60-s simulation. The flow reaches the underside of the superstructure and begins to spill over the deck from the left at $t = 13.5$ s. The horizontal force increases steadily until approximately $t = 18$ s, when the discharge of swash on the right begins to reduce the unbalanced hydrostatic between the two sides of the superstructure. The rising water increases the force to 348.8 kN/m (23.9 kip/ft). In comparison, the vertical force increases rapidly to a maximum of 553.1 kN/m (37.9 kip/ft) during the uprush and then becomes negative.

Hurricane-wave loading on bridge superstructures usually comprises two distinguishable components. First is a short-duration, high-intensity load caused by wave impact, and the second is a slowly varying component associated with the inertia and drag forces. These two components are rather difficult to specify in tsunami loading, considering that a tsunami could be a current of water containing multiple bores and breaking waves. The maximum tsunami loads provided previously are those that consider the impact

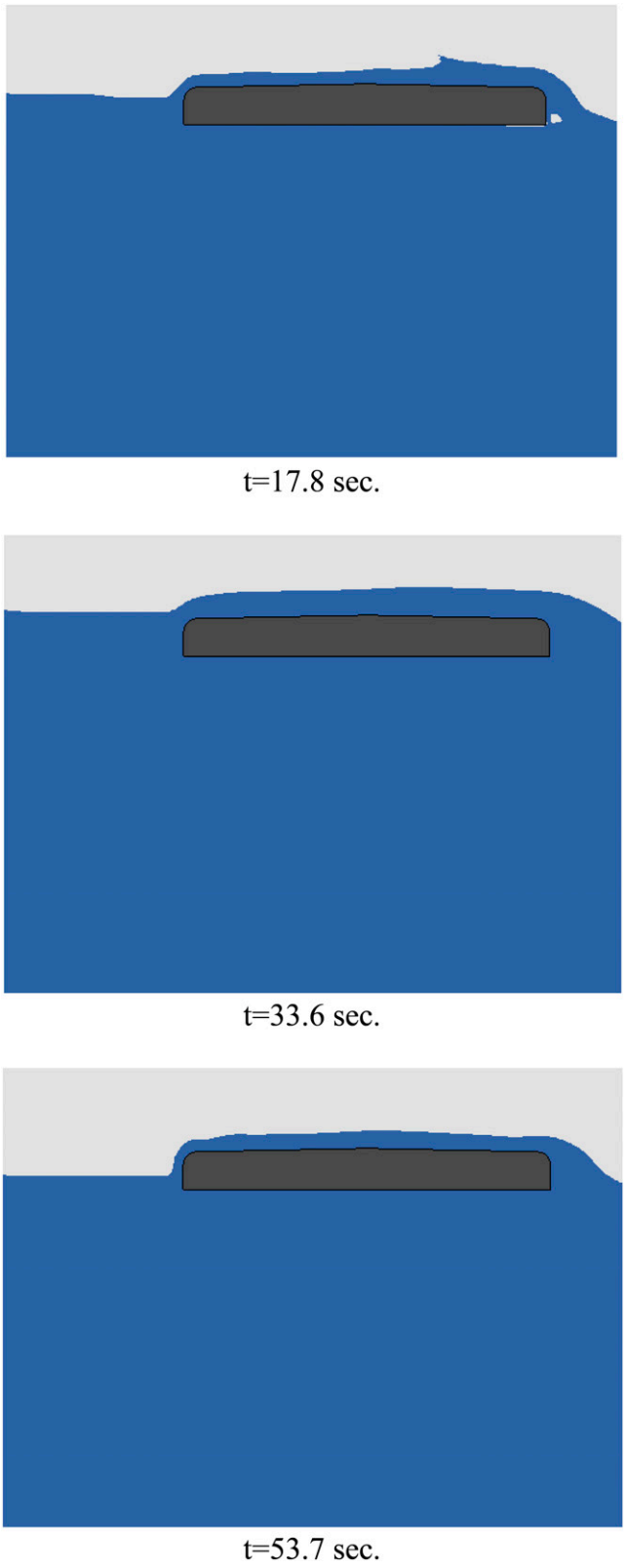

Fig. 9. Screen captures of fluid load simulation

force components. Until large-scale experimental studies show the relative importance of these two components in tsunami loading on bridge superstructures, it is advised that both force components be considered in analysis and design of tsunami-resistant bridges.

The tsunami loads from the finite-element model are compared with other predictions before their implementation in the bridge analysis. Empirical formulas for wave-load prediction are available in AASHTO (2008) and the literature (Bea et al. 1999; Douglass et al. 2006; Cuomo et al. 2009), but are not applicable to tsunamis because of the much longer time and length scales. Because the relatively steady tsunami flow behaves closer to a current in terms of their impact on buildings and structures, the finite-element results can be compared with the AASHTO (2008) design formula for current loads on bridge superstructures. The horizontal drag force is expressed in the form

$$F_{HC} = C_d A \left(\frac{\rho_w}{2}\right) \frac{U_c^2}{1{,}000} \tag{8}$$

where U_c = current speed; A = projected area of superstructure per unit length; and C_d = drag coefficient, taken as 2.5. The formula gives an estimate of 144.5 kN/m (9.9 kip/ft), which is substantially lower than the 348.8 kN/m (23.9 kip/ft) from the finite-element model. The difference might be because of the wave resistance associated with modification of the free surface flow (Duncan 1983). There are no suitable formulas to predict the vertical force on the superstructure. However, the vertical force of 553.1 kN/m (37.9 kip/ft) is reasonable in comparison with the buoyancy force of 270.0 kN/m (18.5 kip/ft), giving the inertia of the rapidly rising water.

Bridge Resistance Analysis

The tsunami loads from FVWAVE and *LS-DYNA* allow assessment of the resistance between the superstructure and substructure against a tsunami generated by a Great Cascadia earthquake. The connections were designed according to the AASHTO (2011) *Guide Specifications for LRFD Seismic Bridge Design* with extreme event limit state and AASHTO (2012) *LRFD Bridge Design Specifications*. All load and resistance factors equal 1.0, and nominal values are used for material strength properties. The horizontal resistance is provided by 24 No. 10 dowel bars at the two abutments, 156 No. 6 dowel bars at the long-column and crown bents, and shear lugs at the two bents over the short spandrel columns. The resistance against vertical loads is provided by the weight of superstructure elements and the pullout capacity of the dowel bars at the long-column bents and the arch crown bent. The superstructure components include prestressed slabs, closure pours, fasciae, drain pipe, bridge rails, and the concrete deck. The dowel bars at the two abutments are ignored, because they are designed for a bearing pad replacement. The bars are separated inside the drilled holes in the prestressed slab ends. Live loads during the event are excluded from the calculation.

A comparison between maximum tsunami-induced horizontal and vertical loads and bridge resisting capacity is provided in Table 1. The resisting capacities are calculated according to the bridge design specifications, in which the limits are based on yielding of the dowel bars and prescribed concrete interface capacity for the shear lugs. When these resisting capacities are exceeded, significant displacement of the bridge superstructure is anticipated. Furthermore, if the tsunami loads are sustained for a long period of time, the ultimate strain in the dowel bars could be surpassed and result in separation between the bridge superstructure and substructure. According to the table, the bridge can resist the maximum tsunami loads generated based on the different scenarios. The horizontal resistance provided by the connection is 3 times greater than the analysis tsunami loading. The vertical resisting capacity is also adequate to resist the tsunami loading, but by a smaller margin. The superstructure of the bridge is relatively

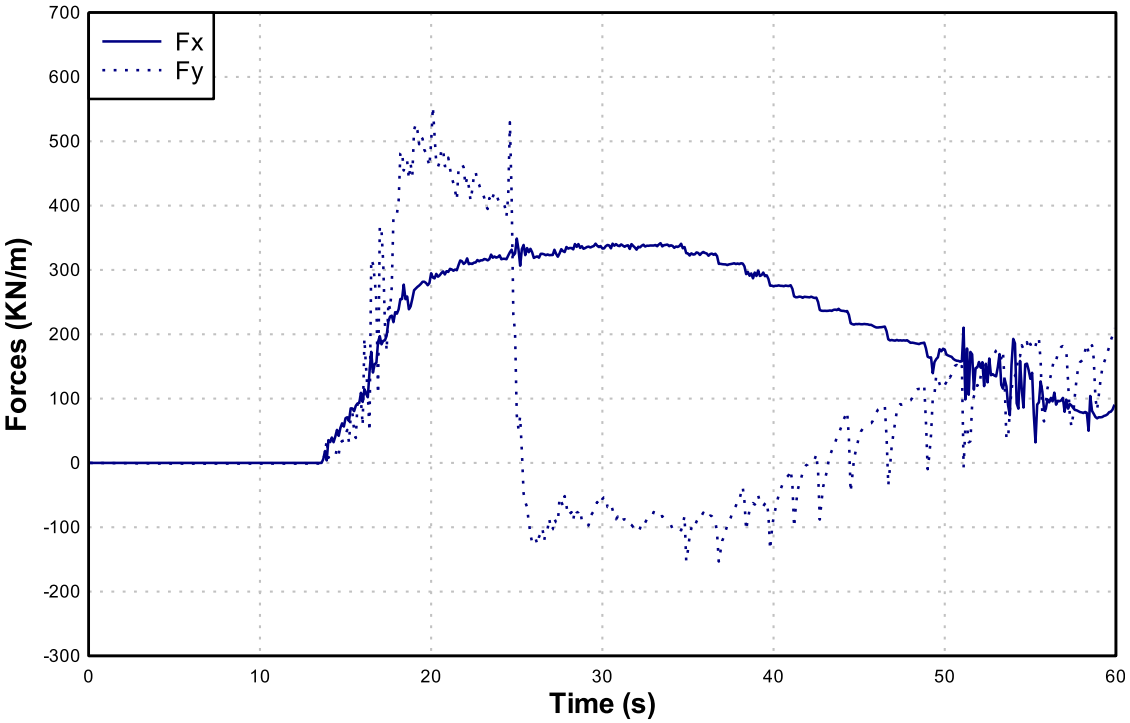

Fig. 10. Tsunami horizontal and vertical forces on the bridge deck

Table 1. Comparison between Maximum Tsunami Loads and Bridge Resisting Capacity

Direction	Maximum tsunami loads [kN/m (kip/ft)]	Bridge resisting capacity [kN/m (kip/ft)]	Design ratio
Horizontal	348.8 (23.9)	1,163.6 (79.7)	3.31
Vertical	553.1 (37.9)	560.6 (38.4)	1.01

thin and light, given its surface area. The superstructure weight contributes 36% to the total vertical capacity. However, when the interaction between the two directional forces or the vertical and horizontal loads is concurrently considered in the capacity comparison, it appears that the connection capacity would not be adequate.

A linear-elastic, finite-element analysis is performed to investigate potential damage to the superstructure. The modeling objective is to observe the displacement of the superstructure caused by the tsunami loads and whether the bridge superstructure reaches the section capacity. Material nonlinearity is not included in the model. The maximum vertical load of 553.1 kN/m (37.9 kip/ft) is divided by the width of the bridge superstructure equal to 15.6 m (51.2 ft), and then the vertical pressure was subtracted by the unit superstructure weight of 13.0 kN/m^2 (0.272 kip/ft^2). The resultant uplift pressure equal to 22.4 kN/m^2 (0.468 kip/ft^2) is applied to the bridge superstructure in the vertical direction. As shown in Fig. 10, a concurrent horizontal load of 291.9 kN/m (20.0 kip/ft) occurs at 20.0 s, the same time as the maximum vertical load. The concurrent horizontal load is simultaneously applied to the model on the side of the superstructure. A deformed shape from the analysis is shown in Fig. 11. Note that the modeling ignores unknown friction forces at the bridge ends and between concrete surfaces at the spandrel column bents. Based on the analysis, a 95-mm (3.75-in.) uplift and 132-mm (5.20-in.) horizontal movement of the superstructure ends are anticipated at the abutments, and the spandrel column bent would rise about 25 mm (1 in.) and move laterally 133 mm (5.25 in.). It is also observed that the arches help resisting the uplift and horizontal movement.

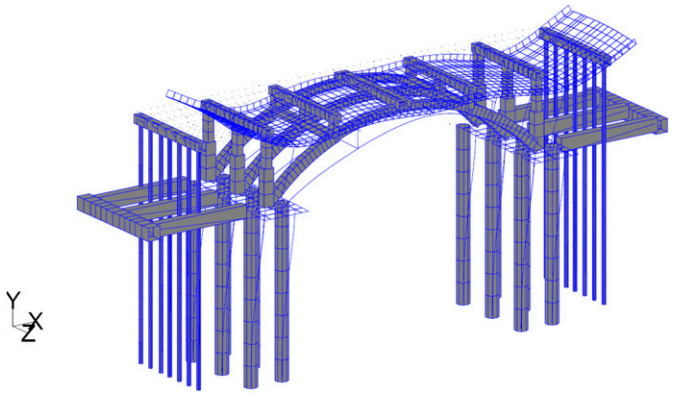

Fig. 11. Deformed shape (50-times magnification) caused by tsunami-induced vertical and horizontal loads

Three critical locations are investigated for potential damage, including positive bending of the deck (prestressing strands in tension) at the long-column bents, negative bending of the deck (deck rebars in tension) near the spandrel column bents, and positive bending of the deck at the arch crown bent. Section capacities are calculated based on the as-constructed plans. All extending prestressing strands are hooked at the interior bents in the closure pour; therefore, the strands are developed in a short distance. Fig. 12 shows bending moment contours occurring in the bridge superstructure under the tsunami-induced vertical and horizontal pressures. As shown in the figure, the bending moment varies across the bridge superstructure over the long-column bents, which are larger near the applied horizontal tsunami load and smaller on the opposite side. The design moment capacity of the section would be overstressed by 25% because of the largest concentrating bending moment. Significant flexural cracking and yielding of the prestressing strands would

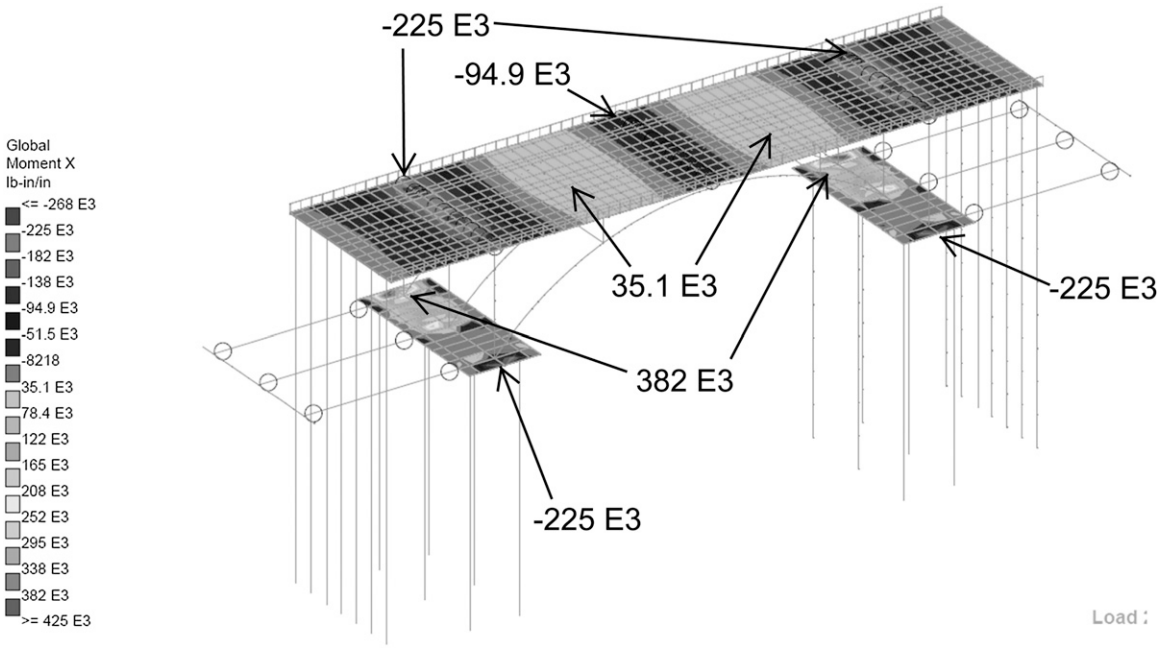

Fig. 12. Bending moment contours generated by tsunami-induced vertical and horizontal loads

occur at this location. Because overall bridge resisting capacities are adequate to resist the tsunami loads, the separation between the superstructure and substructure is not anticipated. The other resisting elements help resisting the loads through the load distribution. The section at the spandrel column bents and at the arch crown bent has adequate capacities with a capacity/applied load ratio of 2.1 and 2.6, respectively. As described, the damage could locally occur in the superstructure, although the bridge superstructure can globally resist the tsunami-induced loads. Fig. 13 shows the new Spencer Creek Bridge, which was constructed and completed recently.

Concluding Remarks

This paper provided tsunami design criteria for coastal infrastructure using a case study of the Spencer Creek Bridge on the U.S. Highway 101 at Newport, Oregon. The process outlined herein is general and applicable to any other facility under wave-body impact situations. The paper presented the horizontal and vertical tsunami loads on the bridge deck. Two tsunami models, COMCOT and FVWAVE, defined the flow fields from three rupture configurations postulated for a Cascadia earthquake. Although both models produce comparable surface elevations at the site, the finite-volume formulation of FVWAVE provides higher flow speed because of its capability to conserve momentum and mass even with formation of tsunami bores. The FVWAVE results define the input to the computational fluid dynamic module of *LS-DYNA*.

In this paper, although base-shear forces induced by wave loads on the typical cross section of the bridge deck are provided, no wave loads on the columns are presented. This is because the two-dimensional model cannot simulate the effects of fluid forces of the flow around the columns, which are necessarily three dimensional.

After comparing the maximum horizontal and vertical tsunami loads with the bridge resisting capacity, it is also concluded that the new Spencer Creek Bridge, which was designed based on the current seismic design provision in the bridge design specifications, is able to resist tsunami loads generated based on different scenarios. The horizontal resisting capacity largely exceeds the tsunami load, but the vertical resisting capacity is just above the tsunami load. Most of the capacity comes from the connections that are not intended to resist the upward vertical loadings, but rather to resist the horizontal loads. The analysis also shows that some structural elements in the superstructure could get damaged locally because of the absence of design requirements for the tsunami loads.

Fig. 13. New Spencer Creek Bridge (image by Solomon C. Yim)

One of the main goals in the bridge design is to keep the superstructure on the supports; therefore, bridges can be used by traffic after natural hazard events. When the tsunami loading criteria are included in the bridge design specifications, the connection and structural element designs are improved and ensure no significant damage and no collapse for bridges in coastal setting caused by tsunami loadings.

Acknowledgments

Partial support from the Oregon DOT (ODOT) under Work Order No. 06-09 to Oregon State University is gratefully acknowledged. The authors thank Professor Kwok Fai Cheung for his comments and suggestions that improved the presentation and layout of the

paper. This publication is also partially funded by the Joint Institute for the Study of the Atmosphere and Ocean (JISAO) under NOAA Cooperative Agreement NA100AR4320148, JISAO Contribution 2182; PMEL Contribution 4087.

References

AASHTO. (2008). *Guide specifications for bridges vulnerable to coastal storms*, Washington, DC.

AASHTO. (2011). *Guide specifications for LRFD seismic bridge design*, 2nd Ed., Washington, DC.

AASHTO. (2012). *LRFD bridge design specifications*, 6th Ed., Washington, DC.

Akiyama, M., Frangopol, D. M., Arai, M., and Koshimura, S. (2012). "Probabilistic assessment of structural performance of bridges under tsunami hazard." *Proc., Structures Congress 2012*, J. Carrato and J. Burns, eds., ASCE, Reston, VA.

Bea, R. G., Xu, T., Stear, J., and Ramos, R. (1999). "Wave forces on decks of offshore platforms." *J. Waterway, Port, Coastal, Ocean Eng.*, 10.1061/(ASCE)0733-950X(1999)125:3(136), 136–144.

Burwell, D., Tolkova, E., and Chawla, A. (2007). "Diffusion and dispersion characterization of a numerical tsunami model." *Ocean Modell.*, 19(1–2), 10–30.

Cheung, K. F., Wei, Y., Yamazaki, Y., and Yim, S. C. (2011). "Modeling of 500-year tsunamis for probabilistic design of coastal infrastructure in the Pacific Northwest." *Coastal Eng.*, 58(10), 970–985.

Clague, J. J. (1997). "Evidence for large earthquakes at the Cascadia subduction zone." *Rev. Geophys.*, 35(4), 439–460.

Cuomo, G., Shimosako, K.-I., and Takahashi, S. (2009). "Wave-in-deck loads on coastal bridges and the role of air." *Coastal Eng.*, 56(8), 793–809.

Douglass, S. L., Chen, Q., and Olsen, J. M. (2006). *Wave forces on bridge decks*, Federal Highway Administration, Washington, DC.

Duncan, J. H. (1983). "The breaking and non-breaking wave resistance of a two-dimensional hydrofoil." *J. Fluid Mech.*, 126, 507–520.

Fritz, H. M., et al. (2012). "The 2011 Japan tsunami current velocity measurements from survivor videos at Kesennuma Bay using LiDAR." *Geophys. Res. Lett.*, 39(7), L00G23.

Goldfinger, C., Nelson, C. H., and Johnson, J. E., and Shipboard Scientific Party. (2003). "Holocene earthquake records from the Cascadia subduction zone and northern San Andreas Fault based on precise dating of offshore turbidites." *Annu. Rev. Earth Planet. Sci.*, 31, 555–577.

Iemura, H., Pradono, M. H., and Takahashi, Y. (2005). "Report on the tsunami damage on the bridges in Banda Aceh and some possible countermeasures." *Proc., 28th JSCE Earthquake Engineering Symp.*, Japan Society of Civil Engineers, Tokyo, 1–10.

Jacoby, G. C., Bunker, D. E., and Benson, B. E. (1997). "Tree-ring evidence for an AD 1700 Cascadia earthquake in Washington and northern Oregon." *Geology*, 25(11), 999–1002.

Kajiura, K. (1970). "Tsunami source, energy and the directivity of wave radiation." *Bull. Earthq. Res. Inst. Univ. Tokyo*, 48, 835–869.

Kataoka, S. (2006). "Scenarios of earthquake and tsunami disaster including damage to road bridges." *Proc., 22th US–Japan Bridge Engineering Workshop*, Public Works Research Institute, Tsukuba, Japan.

Kawashima, K. (2012). "Damage of bridges due to the 2011 Great East Japan Earthquake." *Proc., Int. Symp. on Engineering Lessons Learned from the 2011 Great East Japan Earthquake*, Japan Association of Earthquake Engineering, Tokyo, 82–101.

Kirby, S., Geist, E. L., Lee, W. H. K., Scholl, D., and Blakely, R. (2006). "Tsunami source characterization for western Pacific subduction zones: A preliminary report." *Proc., USGS Tsunami Sources Workshop*, USGS, Washington, DC.

Kosa, K., Nii, S., Miyahara, K., and Shoji, M. (2010). "Experimental study for estimating tsunami forces acting on bridge girders." *Proc., 26th US–Japan Bridge Engineering Workshop*, Public Works Research Institute, Tsukuba, Japan, 1–14.

Kowalik, Z., and Murty, T. S. (1993). "Numerical simulation of two-dimensional tsunami runup." *Mar. Geod.*, 16(2), 87–100.

Liu, P. L.-F., Cho, Y.-S., Briggs, M. J., Kanoglu, U., and Synolakis, C. E. (1995). "Runup of solitary waves on a circular island." *J. Fluid Mech.*, 302, 259–285.

LS-DYNA 971 R5 [Computer software]. Livermore, CA, Livermore Software Technology.

Marks, K. M., and Smith, W. H. F. (2006). "An evaluation of publicly available global bathymetry grids." *Mar. Geophys. Res.*, 27(1), 19–34.

Maruyama, K., Tanaka, Y., and Hosoda, A. (2012). "Damage of bridges structures by huge tsunami and evaluation of tsunami force on bridges." *Proc., 8th Int. Symp. on Social Management Systems, SSMS2012-Disaster Prevention and Reconstruction Management*, United Nations Office for Disaster Risk Reduction, New York, 1–8.

Okada, Y. (1985). "Surface deformation due to shear and tensile faults in a half space." *Bull. Seismol. Soc. Am.*, 75(4), 1135–1154.

Potisuk, T., and McIntier, D. J. (2009). "Coastal connection." *Civil Eng. Mag.*, 79(9), 80–87.

Roeber, V., and Cheung, K. F. (2012). "Boussinesq-type model for energetic breaking waves in fringing reef environment." *Coastal Eng.*, 70, 1–20.

Roeber, V., Cheung, K. F., and Kobayashi, M. H. (2010). "Shock-capturing Boussinesq-type model for nearshore wave processes." *Coastal Eng.*, 57(4), 407–423.

Satake, K., Wang, K., and Atwater, B. F. (2003). "Fault slip and seismic moment of the 1700 Cascadia earthquake inferred from Japanese tsunami descriptions." *J. Geophys. Res.*, 108(B11), 2535.

Sugimoto, T., and Unjoh, S. (2007). "Hydraulic model tests on the bridge structures damaged by tsunami and tidal wave." *Proc., 23th US–Japan Bridge Engineering Workshop*, Public Works Research Institute, Tsukuba, Japan, 1–10.

Titov, V. V., and Synolakis, C. E. (1995). "Modeling of breaking and nonbreaking long-wave evolution and runup using VTCS-2." *J. Waterway, Port, Coastal, Ocean Eng.*, 10.1061/(ASCE)0733-950X(1995)121:6(308), 308–316.

Titov, V. V., and Synolakis, C. E. (1998). "Numerical modeling of tidal wave runup." *J. Waterway, Port, Coastal, Ocean Eng.*, 10.1061/(ASCE)0733-950X(1998)124:4(157), 157–171.

Wei, Y., Cheung, K. F., Curtis, G. D., and McCreery, C. S. (2003). "Inverse algorithm for tsunami forecasts." *J. Waterway, Port, Coastal, Ocean Eng.*, 10.1061/(ASCE)0733-950X(2003)129:2(60), 60–69.

Wei, Y., Mao, X. Z., and Cheung, K. F. (2006). "Well-balanced finite-volume model for long-wave runup." *J. Waterway, Port, Coastal, Ocean Eng.*, 10.1061/(ASCE)0733-950X(2006)132:2(114), 114–124.

Yamazaki, Y., Cheung, K. F., and Kowalik, Z. (2011). "Depth-integrated, non-hydrostatic model with grid nesting for tsunami generation, propagation, and run-up." *Int. J. Numer. Methods Fluids*, 67(12), 2081–2107.

Yamazaki, Y., Cheung, K. F., and Lay, T. (2013). "Modeling of the 2011 Tohoku near-field tsunami from finite-fault inversion of seismic waves." *Bull. Seismol. Soc. Am.*, 103(2b), 1444–1455.

Yamazaki, Y., Kowalik, Z., and Cheung, K. F. (2009). "Depth-integrated, non-hydrostatic model for wave breaking and run-up." *Int. J. Numer. Methods Fluids*, 61(5), 473–497.

Yamazaki, Y., Wei, Y., Cheung, K. F., and Curtis, C. D. (2006). "Forecast of tsunamis generated at the Japan-Kuril-Kamchatka source region." *Nat. Hazards*, 38(3), 411–435.

Yashinsky, M. (2012). "Lessons for Caltrans from the 2011 great Japan earthquake and tsunami." *Proc., Int. Symp. on Engineering Lessons Learned from the 2011 Great East Japan Earthquake*, Japan Association of Earthquake Engineering, Tokyo, 1417–1428.

Yim, S. C., Cheung, K. F., Olsen, M. J., and Yamazaki, Y. (2012). "Tohoku tsunami survey, modeling and probabilistic load estimation applications." *Proc., Int. Symp. on Engineering Lessons Learned from the 2011 Great East Japan Earthquake*, Japan Association of Earthquake Engineering, Tokyo, 430–443.

Yim, S. C., Olsen, M. J., Cheung, K. F., and Azadbakht, M. (2014). "Tsunami modeling, fluid load simulation, and validation using geospatial field data." *J. Struct. Eng.*, 10.1061/(ASCE)ST.1943-541X.0000940, A4014012.

Zhou, J. G., Causon, D. M., Mingham, C. G., and Ingram, D. M. (2001). "The surface gradient method for the treatment of source terms in the shallow-water equations." *J. Comput. Phys.*, 168(1), 1–25.